Journal of Hazardous Materials 211–212 (2012) 304–316

Contents lists available at SciVerse ScienceDirect

Journal of Hazardous Materials

journal homepage: www.elsevier.com/locate/jhazmat

Double-side active TiO_2-modified nanofiltration membranes in continuous flow photocatalytic reactors for effective water purification

G.Em. Romanos[a,*], C.P. Athanasekou[a], F.K. Katsaros[a], N.K. Kanellopoulos[a], D.D. Dionysiou[b], V. Likodimos[a], P. Falaras[a]

[a] Institute of Physical Chemistry, NCSR Demokritos, 153 10 Agia Paraskevi Attikis, Athens, Greece
[b] Department of Civil and Environmental Engineering, University of Cincinnati, Cincinnati, OH 45221-0071, USA

ARTICLE INFO

Article history:
Received 2 June 2011
Received in revised form
19 September 2011
Accepted 20 September 2011
Available online 29 September 2011

Keywords:
NF membranes
Continuous flow
Ultra thin TiO_2 layers
Pollutant photodegradation
Water purification

ABSTRACT

A chemical vapour deposition (CVD) based innovative approach was applied with the purpose to develop composite TiO_2 photocatalytic nanofiltration (NF) membranes. The method involved pyrolytic decomposition of titanium tetraisopropoxide (TTIP) vapor and formation of TiO_2 nanoparticles through homogeneous gas phase reactions and aggregation of the produced intermediate species. The grown nanoparticles diffused and deposited on the surface of γ-alumina NF membrane tubes. The CVD reactor allowed for online monitoring of the carrier gas permeability during the treatment, providing a first insight on the pore efficiency and thickness of the formed photocatalytic layers. In addition, the thin TiO_2 deposits were developed on both membrane sides without sacrificing the high yield rates. Important innovation was also introduced in what concerns the photocatalytic performance evaluation. The membrane efficiency to photo degrade typical water pollutants, was evaluated in a continuous flow water purification device, applying UV irradiation on both membrane sides. The developed composite NF membranes were highly efficient in the decomposition of methyl orange exhibiting low adsorption-fouling tendency and high water permeability.

1. Introduction

The treatment of water and other fluids to remove contaminants is becoming increasingly important. In particular, drinking water may contain hazardous substances such as toxins and endocrine-disrupting compounds [1,2], harmful bacteria and other microorganisms that can cause serious health problems, if ingested by humans or animals. Similarly, untreated wastewater from industrial or agricultural processes usually contains organic pollutants, such as organic dyes, phenols and pesticides, which may be detrimental to heath and/or environmentally damaging. Increasingly stringent regulations for the quality of potable water and the discharge of effluents generate the need for more reliable and sustainable treatment processes, such as highly energy efficient membrane based separation techniques [3]. If the aforementioned benefits could be combined with the development of cost-effective membrane manufacturing methods, this would certainly lead to a rapid growth in the application of membrane technology in wastewater treatment and reuse [4,5].

Specifically, microporous and mesoporous inorganic membranes have attracted considerable attention for water treatment over conventional polymeric membranes [6,7], due to their excellent thermal, chemical, and mechanical stability, and their reusability. Amongst the materials used for the preparation of inorganic membranes, TiO_2 photocatalysts have lately gained tremendous popularity, since a membrane skin layer composed of TiO_2 material allows only small molecules and water to penetrate the membrane pores (i.e., separation function) and simultaneously, its photocatalytic activity causes the decomposition of the larger organic pollutants present in water [8,9]. In this way one of the major problems of membrane separation technology, which is the generation of toxic condensates, can be considerably abated. The photocatalytic activity is also expected to enhance the antibiofouling properties of the membrane, which is one of the main challenges for both research and industry in the field of membrane-based water and wastewater treatment [10,11].

Inorganic membranes generally consist of a macroporous substrate that provides mechanical strength for an overlying thin active layer [12,13]. The usual way to develop the active membrane layer is the sequential dip-coating of the substrate into adequate sols composed of different precursor material, with particles of decreasing size, as we go from the rough support to the active layer. The purpose of this multi-coating procedure is to mask support's

* Corresponding author. Tel.: +30 2106503972; fax: +30 2106511766.
E-mail address: groman@chem.demokritos.gr (G.Em. Romanos).

0304-3894/$ – see front matter © 2011 Elsevier B.V. All rights reserved.
doi:10.1016/j.jhazmat.2011.09.081

defects [14,15] that undermine the integrity of the active top layer. This is time consuming and often results in increased preparation cost and reduced water permeability. Recently, repetition of the dip-coating procedure using a single sol until the desired thickness and homogeneity of the coating layer has been successfully applied for the development of highly efficient TiO_2 membranes [16]. As an alternative to the sol–gel dip coating techniques, chemical vapor deposition using various metal-organic (MO) precursors provides the potentiality to effectively control the pore size by developing active metal-oxide layers on the pore mouth of the rough substrate and/or deposit nanoparticles of very small size that could not be achieved with the usual sol-gel routes. Furthermore, although CVD provides an easily up scalable procedure that has been widely applied for the development of silica based, gas-separating membranes [17–20], it has been scarcely investigated as a method of manufacturing photocatalytic TiO_2 membranes [21]. In fact, up to date, it was principally involved in the formation of thin photoacatalytic layers on non-porous [22,23] or porous substrates in the form of powder [24,25].

In addition, the photocatalytic activity of sol-gel derived TiO_2 membranes was mainly evaluated in batch reactors [2,16,26] and never in a typical cross-flow membrane filtration process. The combination of membrane technology with photocatalysis was solely investigated as the combination of two separated processes in series i.e. photocatalytic action of nanoparticles in suspension followed by membrane filtration [27,28]. Only a few patents have described reactors and water purification devices that involve a membrane as the photocatalytic and filtration component simultaneously [29] and in all these cases, the membrane bears just one-photocatalyticaly active side.

In this work we performed a thorough investigation on the capacity of the CVD method to develop TiO_2 photocatalytic layers on both surfaces of tubular nanofiltration (NF), γ-alumina membranes and we applied these membranes for the photocatalytic degradation of methyl orange in a continuous flow process. The polluted water solution was fed in a specially designed membrane purification device that provided the possibility to effectively illuminate with UV light each membrane surface (external and internal) separately or both simultaneously and operated either in the cross-flow or flow-through membrane mode and pressures up to 16 bar. It was showed that the photodegradation efficiency of the developed membranes was almost doubled when irradiation was applied on both membrane sides and moreover, it was proved that the CVD method, under appropriate CVD reactor conditions, might constitute a cost effective means for the development of composite TiO_2 based inorganic membranes exhibiting high flux and combined photocatalytic, antibiofouling properties.

2. Experimental

2.1. Materials – Chemicals

The supports applied for the development of the TiO_2 deposits were γ-alumina NF membrane tubes with nominal pore size of 5 nm and molecular weight cut off (MWCOT) of 7.5 kD. The nanofiltration layer (1.5 μm in thickness) was located on the external side of the membrane tube, which had a length of 15 cm, ID and OD of 7 and 10 mm respectively and glazed ends of 3 cm length. The rest of the tubular membrane from the external to the internal surface consisted of two intermediate γ-alumina layers and a rough macroporous a-alumina support. Details on the pore size and volume of the several layers can be found elsewhere [30]. The active internal and external surface that was irradiated during the continuous flow and the batch photocatalytic experiments was 20 and 28 cm^2 respectively.

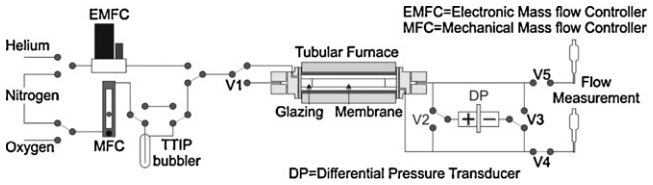

Fig. 1. The prototype CVD reactor applied for the deposition of the TiO_2 layers on the NF membranes.

Titanium tetraisopropoxide (98+% Across 194700010) was used as TiO_2 precursor and Nitrogen gas (99.999) was applied both as the carrier of TTIP vapour and for the measurement of permeability. Oxygen (99.999) was involved as oxidant in the layer-by-layer CVD procedure and helium (99.999) for the measurement of permeability. The methyl orange solution used in the photocatalytic tests had a concentration of 2×10^{-5} M.

2.2. CVD reactor

The prototype reactor applied for the chemical vapor deposition of TiO_2 and for measuring the gas permeability of the membranes is illustrated in Fig. 1. The mechanical mass flow controller (MFC – GPE Limited, 0–1000 ml min^{-1}) was supplied with nitrogen or oxygen and generated a gaseous stream of constant flow rate which, in its dry state or after being enriched with TTIP vapor (bubbler), was introduced inside the reactor from the bore or the annular space of the tubular membrane, depending on the position of the three-way valve (V1). The exhaust valves (V4) and (V5) defined the operation mode (cross-flow or flow-through), while the electronic differential pressure transducer (DP – ABB Transmitter, 2010TD) allowed for on line monitoring the pressure difference between the inner and the outer space of the membrane and vise versa according to the position of the three way valves V2 and V3. The electronic mass flow controller (EMF–Bronkorst, F200CV-FGA-22E) was supplied with nitrogen or helium and was used for the accurate measurement of the permeability at the end of each CVD treatment. The permeability data were acquired with the flow-through technique e.g. all of the gas phase was forced to flow through the pore structure of the membrane with a flow rate varying from 5 to 10 ml min^{-1}.

2.3. CVD conditions and characteristics of the developed TiO_2 membranes

The nitrogen flow rate during all the applied CVD processes was 200 ml min^{-1} and was introduced into the TTIP bubbler at a temperature of (20 °C). No pressure difference was applied during the cross-flow technique whereas the flow through technique was accompanied by pressure differences that started from the level of 80–100 mbar and increased up to the level of 500 mbar during the CVD procedure.

The method of TiO_2 nanoparticles growth and deposition (NPG) proceeded through the pyrolytic decomposition of the TTIP vapor and was performed at a furnace temperature of 600 °C. TTIP vapour exposure and pyrolysis was performed simultaneously.

One of the membranes was modified by NPG deposition, solely with the cross-flow technique (MAl5Ti_2), whereas for two more membranes (MAl5Ti_1, MAl5Ti_3) the cross-flow technique was succeeded by a further treatment with the flow-through technique.

The maximum possible mass (m) of the TiO_2 photocatalytic layers was calculated in accordance to the following equation:

$$m(\text{mg}) = F \times \frac{P_{\text{vap}}}{RT} \times MW \times t \times \frac{1}{1013}\left(\frac{\text{atm}}{\text{mbar}}\right) \times \frac{1}{1000}\left(\frac{\text{L}}{\text{ml}}\right) \times 1000\left(\frac{\text{mg}}{\text{g}}\right) \quad (1)$$

Table 1
Properties of the NPG grown membranes.

CVD technique		MAI5 n/a	MAI5Ti_1 NPG	MAI5Ti_2 NPG	MAI5Ti_3 NPG
Cross-flow outside	Time of treatment	–	640/ < 14	1300/ < 34	960/<24.6
Cross-flow inside	(min)/amount deposited (mg)	–	350/1.7	1060/27.2	1080/27.6
Flow-through outside		–	890/22.8	n/a	600/15.3
Flow-through inside		–	410/10.6	n/a	660/17
Water permeance-UV ($l\,m^{-2}\,h^{-1}\,bar^{-1}$)		0.62 ± 0.02	0.24 ± 0.02	0.37 ± 0.02	
Water permeance-control ($l\,m^{-2}\,h^{-1}\,bar^{-1}$)		0.56 ± 0.01	0.20 ± 0.02	0.30 ± 0.01	
He permeance @ 600 °C ($cm\,s^{-1}$)		13.5 ± 0.3	2.9 ± 0.1	1.7 ± 0.3	1.8 ± 0.1
N_2 permeance @ 600 °C ($cm\,s^{-1}$)		4.5 ± 0.5	1.0 ± 0.1	0.7 ± 0.2	0.69 ± 0.1
Pe (He)/Pe (N_2)		3	2.9	2.43	2.6
Thickness (μm)-external surface			<4.5	<3	<5
Thickness (μm)-internal surface			1.5	2.8	5.5

NPG, nanoparticles growth.

where F ($ml\,min^{-1}$) the flow of nitrogen carrying the TTIP vapor, P_{vap} (mbar) the vapor pressure of TTIP [31,32], $R = 0.08205\,L\,atm\,mol^{-1}\,K^{-1}$, the gas constant, T (K) the temperature of the TTIP bubbler, t (min) the period of treatment (exposure to TTIP vapor) and MW = 79.87 ($g\,mol^{-1}$) the molecular weight of TiO_2.

The calculation of the maximum thickness (d) of the deposited TiO_2 was performed by introducing in the following equation, the geometrical characteristics of the tubular membrane, the solid density (ρ) of TiO_2 and an average porosity ε of 30%:

$$d(\text{ì m}) = 10^4 \left(\sqrt{r^2 + \frac{m}{\rho\pi\ell(1-\varepsilon)}} - r \right) \quad (2)$$

where m (g) the mass of the deposited layer, r (cm) the radius of the tubular membrane and ℓ (cm) the length of the tube.

The temperature profile of the reactor was accurately defined before each CVD treatment (see supporting information). The total hot zone (above 400 °C) was 5 cm and had a 0.5 cm shift from the center towards the exit of the reactor cell, while the temperature measured on the external and internal surface of the membrane along the hot zone of the reactor varied from 420 to 450 °C and from 410 to 442 °C respectively. The temperature of the gas phase sweeping the outer side of the membrane was from 410 to 446 °C whereas, in the inner side, the gas phase temperature was from 415 to 445 °C.

Table 1 pertains to the properties of water and gas permeance of the unmodified and developed TiO_2 membranes as measured in the photocatalytic membrane purification device (see Section 2.4) and the CVD reactor respectively. It also includes information on the maximum possible mass and thickness of the TiO_2 layers as well as the code of the samples that will be used hereinafter to describe the performed experiments.

2.4. Photocatalytic membrane purification device-membrane performance

The photocatalytic membrane purification device comprises a fluid delivery system, the membrane cell unit, the irradiation sources, a pressure transducer, a stream selection three way valve and a backpressure regulator (TESCOM 26-1700 series) mounted at the retentade side of the cell unit. The fluid delivery system consists of a stainless steel fluid transfer vessel equipped with a rodded piston. The piston is driven upwards (delivering fluid) or backwards (priming) by means of a gear motor (BONFIGLIOLI RIDUTTORI S.p.A., VF30 Worm Gearmotor 24 Nm, 0.3 kW), electrically supplied and controlled by an inverter (Mitsubishi, S500E VFD). The minimum and maximum flow rates achieved by installing the appropriate speed reducer are from 0.15 to 15 $ml\,min^{-1}$.

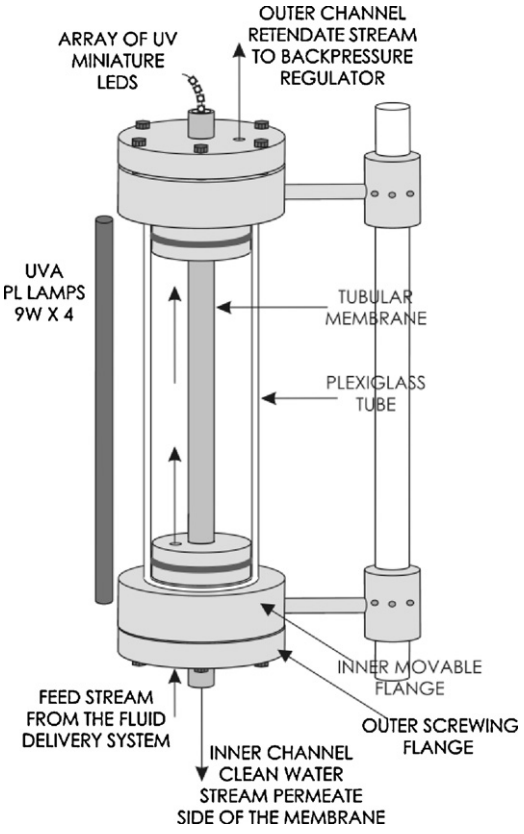

Fig. 2. The unit cell of the photocatalytic purification device with the active TiO_2 modified membrane and the irradiation sources.

The photocatalytic cell unit used in this work is illustrated in Fig. 2. It consists of two concentric tubes placed in the vertical direction. The larger diameter tube is from Plexiglas and has a length of 100 mm and OD, ID of 29 and 21 mm, respectively. The smaller diameter tube is the NF membrane (see Section 2.1) with TiO_2 active porous layers on both its sides. The two tubes define an outer flow channel (the annular space between the tubes) where polluted water is fed and an inner flow channel (internal space of the membrane) where clean water flows out in the downward direction.

The ends of the larger diameter tube are tightly sealed by the inner movable stainless-steel flanges (Fig. 2), via elastomer o-rings placed on a groove around their circumference. The bottom inner flange has a water inlet into the outer flow channel, and the top inner flange has a water outlet from the outer flow channel that leads to the back-pressure regulator. The ends of the inner tube (membrane) are open in air, whereas a tight seal between the

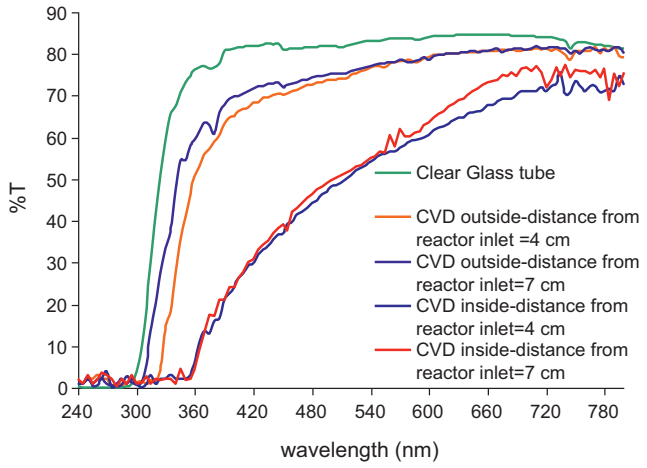

Fig. 3. Transmittance spectrum of the clear borosilicate glass and of the glass tubes with TiO_2 layers on their internal or external surface developed by means of the NPG chemical vapor deposition.

outer channel and the environment is provided by means of the outer screwing stainless-steel flanges that squeeze two o-rings, the one placed in a groove of the inner flange around the glazed ends of the tubular membrane and the other in a groove of the outer flange drilled around the water inlet and outlet bore holes. A more advanced and highly innovative design of the cell unit includes a third flow channel in series with the ones already described. In this additional channel any active photocatalyst, appropriately stabilized in transparent porous photocatalyst carriers like polymer fibers, can be accommodated and effectively irradiated. The high surface area of the porous fibers in combination with the two effective photocatalytic surfaces of the core membrane assures the high efficiency of the overall process. In this advanced configuration the purification device is already applied for a patent to the EPO with the title "Photocatalytic Purification Device" (application number EP10275076.7) [33].

Concerning the light sources, four 9 W UV lamps (Phillips-UVA (PUVA) PL-S/PL-L), placed at a distance of 3 cm from the Plexiglas cell unit, emitting near-UV radiation (315–380 nm) with a peak at 365 nm, were used for irradiating the external surface of the membrane at a light intensity of 2.1 mW cm^{-2}. The inner membrane surface was irradiated by means of an array of 15 UVA miniature leds (TG PURPLE LED Chip LED (3.5 × 2.8), TOYODA GOSEI CO. LTD) emitting near-UV radiation (360–420 nm) with a peak at 383–392 nm at a light intensity of 0.5 mW cm^{-2}.

All the methyl orange (MO) degradation experiments were performed in the cross-flow mode and the concentration of MO solution collected from the retendate and permeate side of the membrane was determined by measuring the visible light absorbance at 466 nm.

Apart from the continuous flow experiments, a batch procedure was also applied to evaluate the photocatalytic efficiency of the developed membranes and especially of the external TiO_2 layer. These experiments were conducted by immersing the TiO_2 membranes into a borosilicate glass reactor containing 25 mL of 20 μM methyl orange. The irradiation on the external surface (2.1 mW cm^{-2}) as well as the analysis of the water aliquots were performed in a way similar to this applied in the continuous flow experiments. The results of the batch experiments were proved valuable in order to define the photocatalytic degradation rate and extract conclusions about the contact time of the pollutant with the active TiO_2 material during the cross flow filtration mode.

2.5. Analytical instruments

Raman measurements were performed in backscattering configuration using a Renishaw inVia Reflex microscope with a high power near infrared (NIR) diode laser (λ = 785 nm, E = 1.58 eV) as excitation source.

A Jeol JSM 7401F Field Emission Scanning Electron Microscope equipped with Gentle Beam mode and the new r-filter was employed to characterize the surface morphology of the developed materials. Gentle Beam technology can reduce charging and improve resolution, signal-to-noise, and beam brightness, especially at low beam voltages (down to 100 V).

A Hitachi U-3010 UV–Visible Spectrophotometer was used for determining the concentration of methyl orange in the aliquots obtained for the batch as well as the continuous flow photocatalytic experiments.

3. Results discussion

3.1. Morphology of the deposited layers

In order to investigate the density and homogeneity of the developed TiO_2 layers as well as the extent of surface coverage, the NPG-cross-flow technique was also involved to modify borosilicate glass tubes at the same conditions as those applied for the Al_2O_3 membranes. In this regard, Fig. 3 presents the UV–vis transmission data of the layers deposited on the glass tubes under the CVD conditions applied for membrane MAl5Ti_2, i.e. cross-flow on the external surface for 1300 min and cross-flow on the internal surface for 1060 min. It should be noted that two glass tubes were used for simulating each of the two surfaces of the membrane and avoid masking of the UV absorbance properties between the externally and internally deposited layers. It can be seen (Fig. 3) that the internal surface was fully and densely covered by TiO_2 nanoparticles that absorbed all of the UV irradiation up to 360 nm. The two spectra obtained for each surface correspond to regions with a longitudinal distance of 3 cm between each other extending in the hot zone of the reactor. It can be concluded that deposition was uniform on the internal side of the glass tube along the length of the reactor something that does not hold on the external side where deposition declines significantly towards the outlet of the reactor.

Fig. 4 shows the Raman spectra obtained on both surfaces of the modified membrane MAl5Ti_2 at a region corresponding to the center of the CVD reactor. The Raman active modes of the anatase

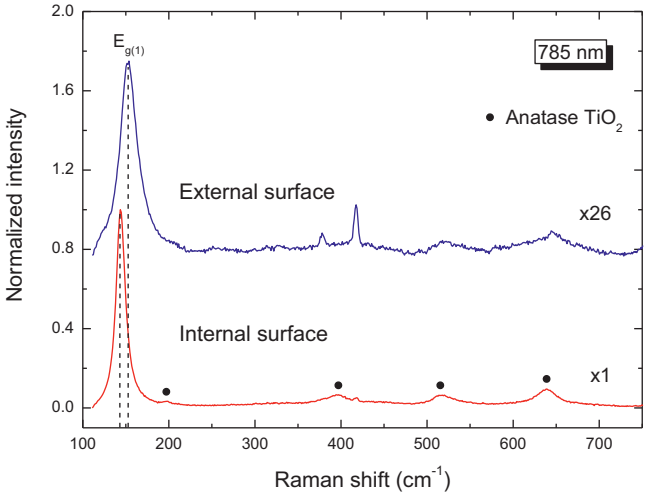

Fig. 4. Raman spectra on the external and internal surfaces of the MAl5Ti_2 membrane at 785 nm. Dots depict the anatase TiO_2 Raman modes.

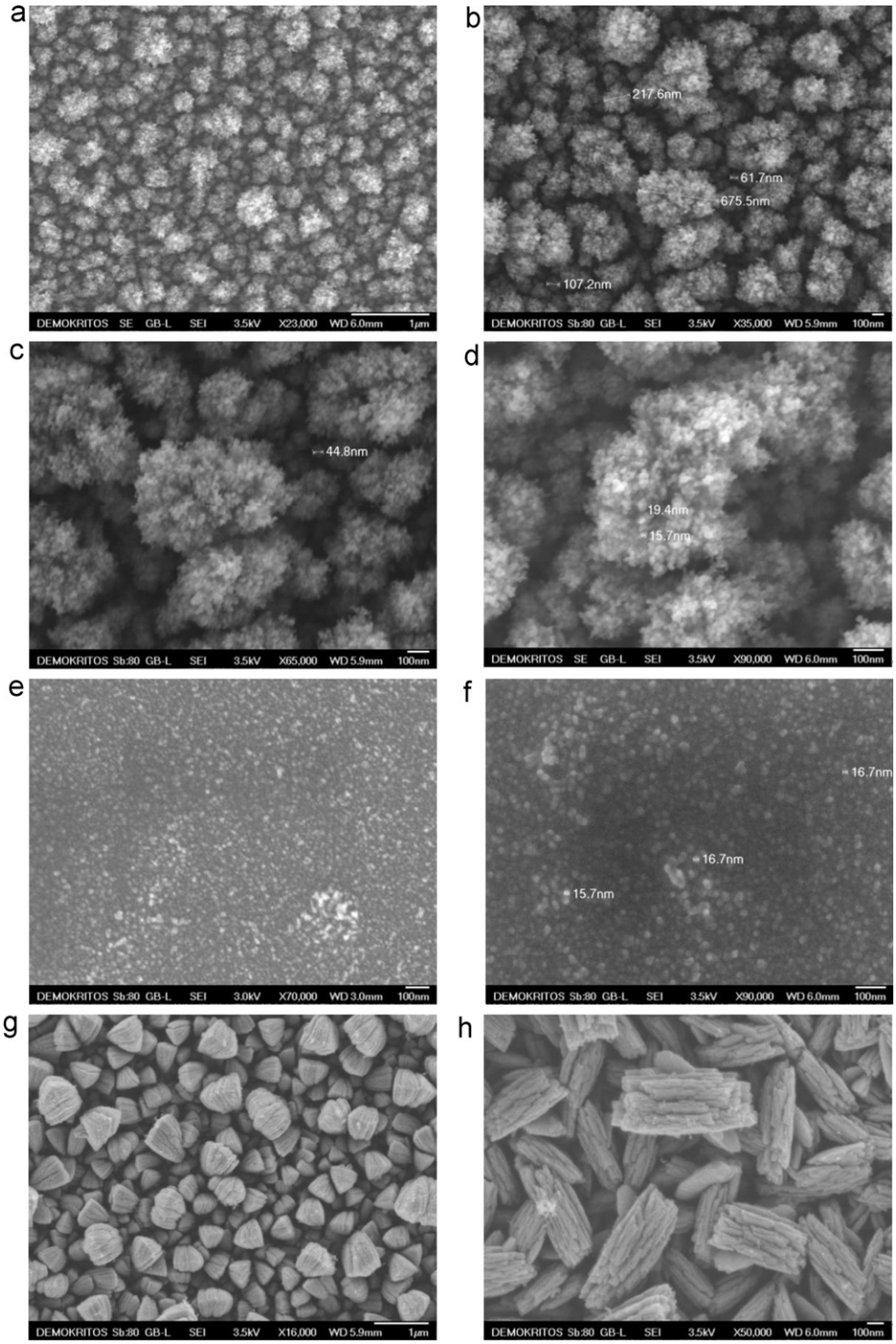

Fig. 5. SEM images of the TiO_2 layers deposited on silicon wafers: (a, c) Deposition at a distance of 35 mm from the reactor inlet on the internal surface and cross-flow mode. (b, d) Deposition at a distance of 65 mm from the reactor inlet on the internal surface and cross-flow mode. (e, f) Deposition at distances of 35 and 65 mm from the reactor inlet on the external surface and cross-flow. (g, h) Deposition at distances of 35 and 65 mm from the reactor inlet on the external surface and flow-through.

phase, which is the most photocatalytically active TiO_2 phase, were clearly identified on the internal side of the membrane. However, the intensity of the anatase Raman peaks decreased markedly for the external membrane side, supporting the sparse deposition of TiO_2 nanoparticles. The Raman intensity reduction was further accompanied by significant shift and broadening, most prominent for the low frequency E_g anatase mode. The latter band shifted from 145 to 152 cm^{-1}, while its full-width at half-maximum (FWHM) increased from 12 to 25 cm^{-1} for the internal and external membrane faces, respectively. This variation can be primarily explained by the optical phonon confinement effect, resulting in both broadening and blue shift of the Raman modes in nanosized materials [34]. Based on these values and the linear scaling of the Raman shift vs FWHM derived from the phonon confinement effect [35], a

decrease of the anatase nanoparticle size from approximately 11 to 5 nm can be inferred for the titania deposition on the internal and external membrane sides.

Furthermore, in order to investigate the morphology of the TiO_2 deposits developed during the NPG-flow-through technique, small pieces of silicon wafers were placed at different distances along the length of a membrane and analysed with SEM after the CVD treatment. For elucidating the morphology of the internally deposited nanoparticles, the silicon wafers were laid along the internal side of the membrane tube whereas, for the investigations concerning the morphology of the external deposition the silicon wafers were cemented on the external surface by means of a special graphitic adhesive (AREMCO GRAPHI-BOND 669). In this case the CVD conditions were similar to those applied for membrane MAl5Ti_2 with the cross-flow technique and for membrane MAl5Ti_1 with the flow-through technique. Fig. 5a, c and b, d, present the SEM images of the silicon wafers that were located internally at a distance of 35 and 65 mm from the inlet of the reactor respectively and treated sequentially with the cross-flow and flow-through techniques. The uniformity of the internal deposition along the length of the reactor is once again evidenced. In Fig. 5c, d we can distinguish a subjacent layer consisting of TiO_2 nanoparticles with a uniform diameter of about 40–60 nm covered by large but not densely deposited particles of size around 500 nm.

The deposition has a granular structure revealing that both particles and precursor were deposited. The larger particles were formed during the flow-through treatment and started to grow in expense of a uniform layer of smaller particles due to diffusion limitations; i.e. protruding entities into the particles boundary layer grow at the expense of their neighbors since they are able to catch more of the reactants from the gas stream.

In Fig. 5e, f we present the deposition structure on the externally located wafers treated in the cross-flow mode at distances of 35 and 65 mm from the inlet of the reactor. In this case, due to the counter acting thermophoretic effect (see also Section 3.2), only small diffusion particles of size <20 nm were deposited. Further treatment in the flow-trough mode led to the structures observed in Fig. 5g, h. It can be seen that the morphology of these deposits is far from granular (the vapor is totally consumed in gas phase reactions) and seem to consist of large particles grown through collisions between the smaller ones in the gas phase. Moreover the morphology differs considerably for a distance of 3 cm along the length of the reactor revealing the inhomogeneity of the externally deposited layers.

3.2. Effect of the TiO_2 deposit morphology on the gas permeability

As already shown by the SEM analysis (Fig. 5e, f), the NPG deposition on the external surface of the membranes during the NPG-cross-flow technique resulted to the formation of porous layers, consisting of very small diffusing TiO_2 nanoparticles that, had a size below the threshold of 20 nm. It can be stated that due to the much smaller dimension of the membrane nanopores (5 nm), the NPG deposition occurred just on the top surface of the externally located NF layer (diffusing particles had no access to the NF pore structure). On the other hand, the internal rough support exhibits a macropore structure with a pore size around 2 μm [30] that allows for the infiltration of larger (>50 nm) thermophoretic nanoparticles, at least during the initial stages of the CVD treatment. From the size of the TiO_2 nanoparticles that deposit on the external surface it is possible to approximately estimate the pore size of the formed NPG layer (one third of the particle size [36]), 5 nm, which is almost identical to this of the subjacent γ-alumina NF layer. As a consequence the pores of the γ-alumina NF layer remain unaffected and the gas diffusion through the entire membrane is co-operatively controlled form both nanoporous layers, e.g. the already existing γ-alumina and the CVD deposited TiO_2 layer.

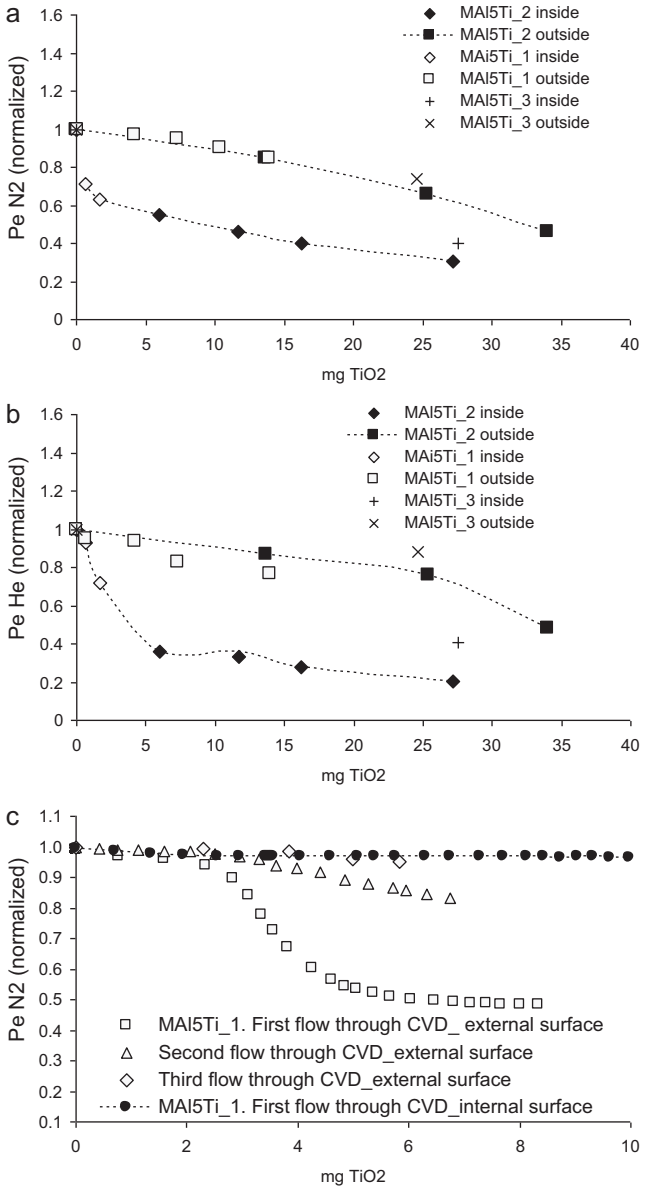

Fig. 6. Permeability evolution vs the amount of TiO_2 deposit, after and during the CVD modification for the three TiO_2 membranes MAl5Ti_1, MAl5Ti_2 and MAl5Ti_3, (a) Nitrogen in the cross-flow mode, (b) Helium in the cross-flow, (c) Nitrogen in the flow-through technique.

Fig. 6 give an overview of the permeance evolution during the CVD for the three membranes developed with the NPG approach. The values of the *x*-axis represent the maximum possible mass (m) of each TiO_2 photocatalytic layer and were calculated in accordance Eq. (1).

The gas permeance in (mol m^{-2} s^{-1} Pa^{-1}) was calculated according to the following equation:

$$\mathrm{Pe} = \frac{F}{S\Delta P} \times \frac{T_{\mathrm{stand}}}{T_{\mathrm{meas}}} \times \frac{P_{\mathrm{meas}}}{P_{\mathrm{stand}}} \times \frac{1}{60}\left(\frac{\mathrm{min}}{\mathrm{s}}\right) \times \frac{1}{22,400}\left(\frac{\mathrm{mol}}{\mathrm{ml}}\right) \times 10^4\left(\frac{\mathrm{cm}^2}{\mathrm{m}^2}\right) \times \frac{1}{100}\left(\frac{\mathrm{mbar}}{\mathrm{Pa}}\right) \quad (3)$$

where F (ml min^{-1}) the gas flow measured at the permeate side of the membrane, S (cm^2) the active surface of the membrane, ΔP (mbar) the pressure difference between the retendate and permeate side of the membrane, T_{meas} (K) and P_{meas} (atm) the temperature and pressure at which the flow was measured and T_{stand} (K) and

P_{stand} (atm) the standard conditions 273 K and 1 atm. The decrease of the gas permeance during the deposition on the external surface can be mainly attributed to the reduction of the starting surface porosity and the contribution of an additional higher resistance to the overall gas flow rather than to narrowing of the already existing pores. This is further supported by the results presented in Table 1, where it can be seen that the He over N_2 permeance ratio after the CVD modification still resides in the Knudsen regime, indicating that the pores of the diffusion controlling layers are in the mesopore region (2–50 nm).

Fig. 6a and b present the N_2 and He permeability results that were obtained after the completion of each CVD cycle (ex-situ) in the cross-flow mode. It can be observed that the dependence of nitrogen and helium permeance on the amount of deposited TiO_2 (or time of treatment) for the three modified membranes shows an almost similar trend, a fact indicating the repeatability of the NPG modification technique. However there exist some deviations, especially between membranes MAl5Ti_2 and MAl5Ti_3, which can be attributed to the fact that membrane MAl5Ti_3 was continuously treated up to the deposition of a total TiO_2 amount of about 25 mg without intermediate interruptions of the CVD procedure for measuring the permeability, as was the case for membrane MAl5Ti_2. A second reason for the deviation is that the starting, unmodified g-Alumina membrane cannot be exactly the same material in all the CVD modifications. These also explain the identical permeance values of membranes MAl5Ti_2 and MAl5Ti_3. Although MAl5Ti_3 has been coated by both cross-flow and flow-through methods and has more deposited TiO_2 comparing to MAl5Ti_2 (Table 1) it exhibits identical permeance values with membrane MAl5Ti_2.

An interesting remark coming up from Fig. 6a and b is that the CVD treatment in the cross-flow mode is accompanied by a gas permeance reduction, which is much more pronounced when the nanoparticles deposition occurred on the internal surface of the membrane. Specifically, deposition seems to be more effective during the initial stages of the CVD treatment on the internal side. This is due to the combined effect of various factors like the different temperature between the membrane surface and the sweeping gas phase and the different pore size between the NF layer (external) and the rough macroporous support (internal).

It must be noticed that in the inner membrane side, the TTIP vapor is not entirely consumed in homogeneous gas phase reactions due to the relatively moderate temperature of the sweeping gas (445 °C). Thereby both vapor and particles are deposited (see also Fig. 5a and b). In this mixed type of deposition, the vapor acts as a binding agent and makes the layer denser as compared to pure particle deposition. Moreover due to the temperature difference between the gas phase (445 °C) and the internal membrane surface (442 °C), all the grown in the gas phase nanoparticles, independently of their size, are deposited on the surface under the influence of a positively acting thermophoretic driving force. These particles are capable to enter the pore structure of the macroporous support and effectively block the pores leading to a considerable reduction of the permeability during the initial stages of the treatment. As soon as there is no further access to the macropore structure, the newly produced nanoparticles continue to deposit on the top surface forming an external layer and for this reason the rate of permeance reduction becomes slower (see Fig. 6a and b). Moreover since the TTIP vapor is not totally consumed in homogeneous gas phase reactions, leaf-like structures are formed, which act as adsorption sites for the unreacted vapor and start to grow in expense of the layer formation (Fig. 5a and b). On the other hand, the higher temperature of the external membrane's surface (450 °C), compared to this of the gas phase that swept the annular space of the reactor (446 °C), generated a counter acting to the deposition thermophoretic phenomenon. Only particles exhibiting high diffusion velocity (small size particles) could overcome the competitive thermophoretic driving force (−4 °C or ∇T = 10 K/cm) and deposit on the membrane. Thermophoresis holds for particle size below the mean free path of the surrounding gas molecules, which is about 180 nm for N_2 at 1 atm and 773 K. More specific, the thermophoretic velocity (Vth) was calculated through the following equation [37]:

$$V_{th} = \frac{-0.55\eta\nabla T}{\rho_g T} \quad (4)$$

where η the gas viscosity (Pa s) and ρ_g the gas density (kg m^{-3}) and was found to be 6×10^{-5} m s^{-1} for particle size from 5 to 170 nm. Thereby, diffusion velocities well above 6×10^{-5} m s^{-1} were required for deposition to occur and this is translated to particle sizes of well below 20 nm [22,37,38]. In this context it is stated that most of the formed nanoparticles continued to grow through collisions and were further deposited downstream in the cold area of the reactor outlet and only a very small portion of them (diffusion particles with size <20 nm) reached the membrane surface. Moreover, a fraction of these diffusing particles was deposited on the walls of the reactor. For these reasons the permeance decline as a function of time was smooth, even from the beginning of a cross-flow treatment on the external surface of the membrane.

The evolution of nitrogen permeance during the subsequent flow-through treatment is presented in Fig. 6c. It should be noted that the NPG-flow-through modification was applied for two membranes (MAl5Ti_1 and MAl5Ti_3), as a continuation of the cross-flow and for this reason the permeance evolution results obtained during the treatment are further discussed by taking also into account the morphological characteristics of the already deposited TiO_2 layers. In this regard the flow-through technique did not considerably altered the way of deposition in the internal side of the membrane (Fig. 6c, curve MAl5Ti_1 inside) and permeance continued to drop by about 3% for every 2 mg of deposited TiO_2. This rate however was lower than this obtained during the last treatment with the cross-flow technique, 4.5% (Fig. 5a, curve MAl5Ti_2 inside), an issue revealing that with the application of a differential pressure, a portion of the TTIP vapour which enters in the reactor, attains to penetrate through the substrate pores, before been pyrolytically decomposed, and is further consumed into surface reactions onto the pore walls of the subsequent macroporous layers. The as formed ultra thin layers on the macropore walls have not significant effect on the permeance.

Contrary, during the flow-through modification on the external surface, the effect of deposition on the permeance was very intense, especially in the first treatment (Fig. 6c curve MAl5Ti_1 outside). This was the result of a significant increase in the amount of deposited nanoparticles (both diffusing particles and larger ones are deposited) and moreover, it may be the case that a complete monolayer of TiO_2 nanoparticles covering the entire NF surface was for the first time accomplished. From the results of Table 1 it can be observed that at the end of the last CVD treatment with the cross-flow technique (MAl5Ti_1), the total deposited mass of TiO_2 on the external surface was 14 mg. With the assumption of a 30% open porosity, this mass corresponds to a layer thickness of about 1.7 μm (Eq. (2)).

However, the average particle size was <20 nm. The much higher calculated thickness compared to the nanoparticle size indicates that upon completion of the cross-flow treatment for membrane MAl5Ti_1, a few tenths of nanoparticle layers must have been formed. However, from the permeance evolution during the cross-flow, as well as from the UV–vis transmittance spectrum (Fig. 3), it can be concluded that the deposition was inhomogeneous along the length of the reactor and that there were uncovered regions of the membrane surface close to the reactor's outlet, which were completely covered during the first run with the flow-through technique.

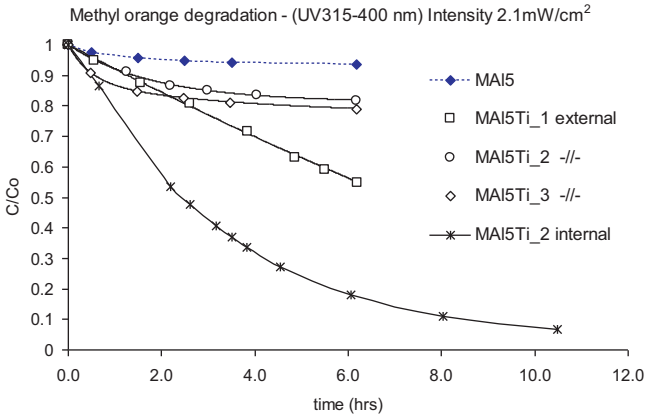

Fig. 7. Efficiency of the composite TiO_2 NF membranes to photodegrade MO in the batch mode.

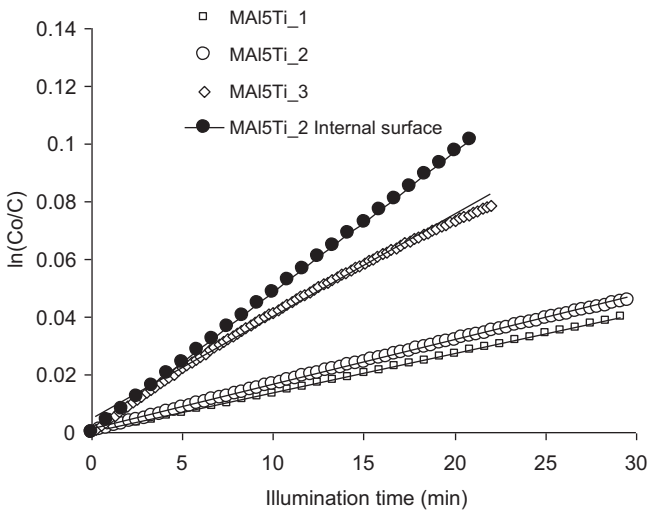

Fig. 8. Photodegradation kinetics of methyl orange expressed by $\ln(C_o/C)$ vs time plots for the different membranes.

3.3. Photocatalysis

3.3.1. Batch experiments – Extraction of the reaction rate constants

The photocatalytic activity of the developed TiO_2 membranes in the batch mode was evaluated in terms of methyl orange (MO) dye decomposition as shown in Fig. 7. It must be noted that during the batch experiments, the light sources irradiated just the external surface of the examined membranes. For this reason discussions concerning the degradation results are mainly restricted to the different morphology of the externally deposited TiO_2 layers. In what concerns the photocatalytic activity of the internal layer, this was examined with a borosilicate glass tube, internally modified under the conditions applied for membrane MAl5Ti_2 (see Table 1).

3.3.2. Photocatalytic efficiency of the external surface

Compared to the unmodified γ-alumina membrane (MAl5), the external surface of the NPG derived TiO_2/UV photocatalytic membranes was much more efficient in decolorizing the initial orange color of MO within 6 h (Fig. 7). In the first instance, from the results presented in Fig. 7 it can be concluded that the efficiency of the external surface of the TiO_2 membranes MAl5Ti_2 and MAl5Ti_3 within 3 and 6 h under irradiation, was analogous to the amount of the deposited TiO_2, which was 34 and 40 mg respectively (Table 1). However, MAl5Ti_1 constitutes an exception to this rule, since with 37 mg of deposited TiO_2 it has photo degraded higher amounts of methyl orange within the respective periods.

Since there was not correlation between the deposited amount and the degradation efficiency, the results were further interpreted in relation to the morphological characteristics of the externally deposited layers. The examination of the reaction kinetics assisted in this direction. To this effect, the destruction rate of the MO photocatalytic oxidation was fitted with the Langmuir–Hinshelwood (L–H) kinetics model [39,40].

The experimental conditions such as the reactor volume the pH, the photo intensity and the initial concentration C_o of the solution were identical for all the tested membranes. Moreover at the early stages of the photocatalytic process any changes such as intermediates effects or pH alteration had been considered as negligible and due to the very small concentration of the pollutant (20 μM solution) the L–H equation was simplified to an apparent first-order equation [41]:

$$\ln\left(\frac{C_o}{C}\right) = k_r K t = k_{app} t \quad (5)$$

where C (mg l^{-1}) the concentration of the reactant, t the illumination time (min), k_r the constant of reaction rate (mg l^{-1} min^{-1}), K the adsorption constant of the reactant (l mg^{-1}) and k_{app} the pseudo first-order apparent constant (min^{-1}). The plots of $\ln(C_o/C)$ versus time in Fig. 8 represent a straight line. The slope of linear regression equals to the apparent first-order rate constant. The values corresponding to the developed membranes are presented in Table 2. Examination of the reaction kinetics in regard to the mass of the deposited layers and the way of deposition led to the conclusion that apart from the amount of the deposited photocatalyst, porosity and effective illumination are also crucial factors for the development of highly efficient photocatalytic ultrafiltration membranes.

More specific, during the beginning of the photocatalytic process, MAl5Ti_2 exhibited higher reaction rate than MAl5Ti_1, even though the TiO_2 deposited amount was lower than this of membrane MAl5Ti_1.Despite the fact that the TiO_2 mass which is sufficient for the formation of a complete monolayer of small nanoparticles (<20 nm) is about 0.2 mg (calculated according to Eq. (4) for a layer thickness of 20 nm), the permeance evolution during the CVD in combination with the UV–vis transmittance data have already evidenced that the surface of membrane MAl5Ti_2, with 34 mg of deposited TiO_2, is partially covered. The deposition consists of multi-layers of small nanoparticles (<20 nm), the number of the layers declining towards the end side of the membrane (outlet of the CVD reactor). In this regard there must be extended areas on the membrane's surface, especially near its center, covered by highly active small dimension nanoparticles (Fig. 5e) that can be effectively illuminated due to the small number of the formed layers.

Similarly, membrane MAl5Ti_1 underwent partial coverage of its surface during the cross-flow modification (14 mg). However the layers of the highly active small nanoparticles were fully covered by additional layers of larger, overgrown particles, (see Fig. 5g, h), deposited during the subsequent flow-through modification (22.8 mg). In this way, the highly active small, deposited under diffusion control, nanoparticles were not efficiently irradiated and the degradation of MO was the result of the photocatalytic activity of just the larger ones. In spite of this, long after the beginning of the illuminating degradation experiment, the activity of membrane MAl5Ti_1 overtakes this of membrane MAl5Ti_2 as a consequence of the higher amount of deposited photocatalyst.

Membrane MAl5Ti_3 with 24.6 mg and 15 mg of TiO_2 during the cross-flow and flow-through modification respectively, exhibited the faster reaction rate amongst the three membranes. Compared to membrane MAl5Ti_1, membrane MAl5Ti_3 possessed higher amount of TiO_2 deposited during the cross-flow modification. In

Table 2
Apparent reaction constants for the NPG developed membranes.

	$k_{app} \times 10^3$ (min^{-1})	R^2	Mass TiO_2 (mg) cross-flow	Mass TiO_2 (mg) flow-through
MAl5Ti_1	1.37	0.999	14	22.8
MAl5Ti_2	1.55	0.999	25	n/a
MAl5Ti_3	3.55	0.994	24.6	15.3
MAl5Ti_2 Internal surface	4.9	0.999	22.6	n/a

this respect the layers of the small diffusion particles are not fully covered by larger ones and consequently they are still effectively irradiated. The higher reaction rate compared to membrane MAl5Ti_1 is attributed to the higher amount of small nanoparticles that are effectively irradiated and compared to membrane MAl5Ti_2, the higher reaction rate is attributed to the higher total amount of deposition.

3.3.3. *Photocatalytic efficiency of the internal surface*

What is important to note is the very different photocatalytic activity between the internal and external surface of membrane MAl5Ti_2. Although the period of CVD treatment inside and outside of the tubular membrane was identical, the internally deposited layer exhibited 3 times faster photodegradation rate during the initial stages of the test and 4.5 times higher photodegradation capacity after 6 h of illumination (Fig. 7). This large difference cannot be attributed to the different morphology of the deposited layers as already concluded by the SEM analysis (Fig. 5). It is rather the TiO_2 mass/reaction volume ratio that causes this enhanced differentiation.

Indeed as already discussed in Section 3.2, the amount of TiO_2 deposited on the external surface should be much lower than this calculated by means of Eq. (2), since a fraction of the particles formed in the gas phase (the thermophoretic ones) are lost downstream the reactor and/or are deposited on the reactor walls. In this case the crucial contribution of the photocatalyst amount to the photodegradation efficiency of the membrane is evidenced.

3.4. *Photocatalysis – Continuous flow experiments*

3.4.1. *Irradiation of the internal surface*

The efficiency of the internal surface of the modified membranes MAl5Ti_1 and MAL5Ti_2 to photocatalyticaly degrade MO in a continuous flow process is shown in Fig. 9a, b. The irradiation characteristics are already described in Section 2.4. The figures also pertain to the results obtained in dark conditions for the unmodified membrane MAl5 and the modified membranes MAl5Ti_1, MAL5Ti_2, as well as to the results obtained for the unmodified membrane MAl5 under illumination. Furthermore, Fig. 9c, d illustrates the percentage of MO removed from the 20 μM solution either by photolysis, adsorption and photodegradation as a function of the total volume of the contaminated water feed. This percentage was calculated from (Eq. (6a)), whereas the net amount of the MO removed (mg) was extracted from the mass balance equation (Eq. (6b)) as following:

$$A\% = \left(1 - \frac{\sum_{i=0}^{t} (V_{per})_i (C_{per})_i - \sum_{i=0}^{t} (V_{ret})_i (C_{ret})_i}{\int_0^t C_{feed} F_w t dt} \right) \quad (6a)$$

$$A\,(\text{mg}) = 10^{-3} \left(\int_0^t C_{feed} F_w t dt - \sum_{i=0}^{t} (V_{per})_i (C_{per})_i - \sum_{i=0}^{t} (V_{ret})_i (C_{ret})_i \right) \quad (6b)$$

where F_w (ml min^{-1}) the constant flow rate of the fluid delivery system, t (min) the time elapsed from the start of the experiment, $(V_{per})_i$ and $(V_{ret})_i$ (ml), the liquid volume collected from the permeate and retendate side at the specific time interval and $(C_{per})_i$ and $(C_{ret})_i$ (ppm) the corresponding MO concentrations.

A first remark (Fig. 9a, b) is that in the absence of irradiation, the modified membranes (MAl5Ti_1 and MAl5Ti_2 control) exhibited higher efficiency to remove MO from water when compared with the unmodified membrane (MAl5-control, MAl5 UV inside).

More specific, the concentration of the methyl orange at the permeate side of the modified membranes under dark was reduced to the 90% of the feed, while the respective retention for the unmodified membrane was 98% in dark and 94% under illumination (photolysis of MO). From these differences and especially by interpreting the results presented in Fig. 9c, d it is possible to discriminate the fraction of methyl orange removed due to photolysis and due to adsorption on the alumina substrate and extract the net amount of the pollutant that was photodegraded or adsorbed on the TiO_2 surface.

It must be noted that, electrostatic repulsion or size exclusion are not considered as possible mechanisms of MO removal since the plots of MO concentration in the retendate side of the membranes (Fig. 9e, f) did not showed any attribute of pollutant condensation (the normalised concentration is in the range 0.98–1.08). The calculated amounts of removed MO are presented in Table 3 together with the conditions of the continuous flow process that was applied for each membrane. By taking into account that the maximum total TiO_2 mass deposited on both sides of each modified membrane was about 50 mg (Table 3) it was possible to calculate the net methyl orange adsorption capacity of the developed TiO_2 layers up to the 150 ml and 250 ml volume of polluted water feed. This was 4×10^{-4} and 5.2×10^{-4} g g^{-1} for membrane MAl5Ti_1 and 3.1×10^{-4} and 4.6×10^{-4} g g^{-1} for membrane MAl5Ti_2 respectively.

This difference and especially the contradicting fact that MAl5Ti_2 with a higher amount of smaller nanoparticles and a more extended porosity (Section 3.2) exhibited lower adsorption capacity, leads to the conclusion that adsorption occurred solely on the external surface, as expected, due to the absence of UV irradiation. Indeed, when normalising the adsorbed MO amount over the externally deposited TiO_2 mass, the adsorption capacity of membrane MAl5Ti_2 is 6×10^{-4} and 8.6×10^{-4} g g^{-1} compared to the values of 5.2×10^{-4} and 6.8×10^{-4} for membrane MAl5Ti_1.

The effect of adsorption on the external TiO_2 layer is also evidenced in Fig. 9b. It can be seen that during the first illumination test with membrane MAl5Ti_2, the concentration of methyl orange at the permeate side increased suddenly after a permeate volume of about 50 ml. At this point, the pollutant molecules have occupied the entire active centers of the externally deposited TiO_2 and MO removal continues solely as the result of the photocatalytic degradation on the internal surface. The second photocatalytic test on membrane MAl5T_2 (Fig. 9b) was performed after washing the membrane with a certain volume (100 ml) of pure water with the purpose to remove the adsorbed MO molecules. It can be seen that the pollutant concentration at the permeate side during this second run was at the level of the end of the first run, (when MO adsorption was completed), a fact revealing that washing with water was inadequate for efficient MO desorption. However a small fraction

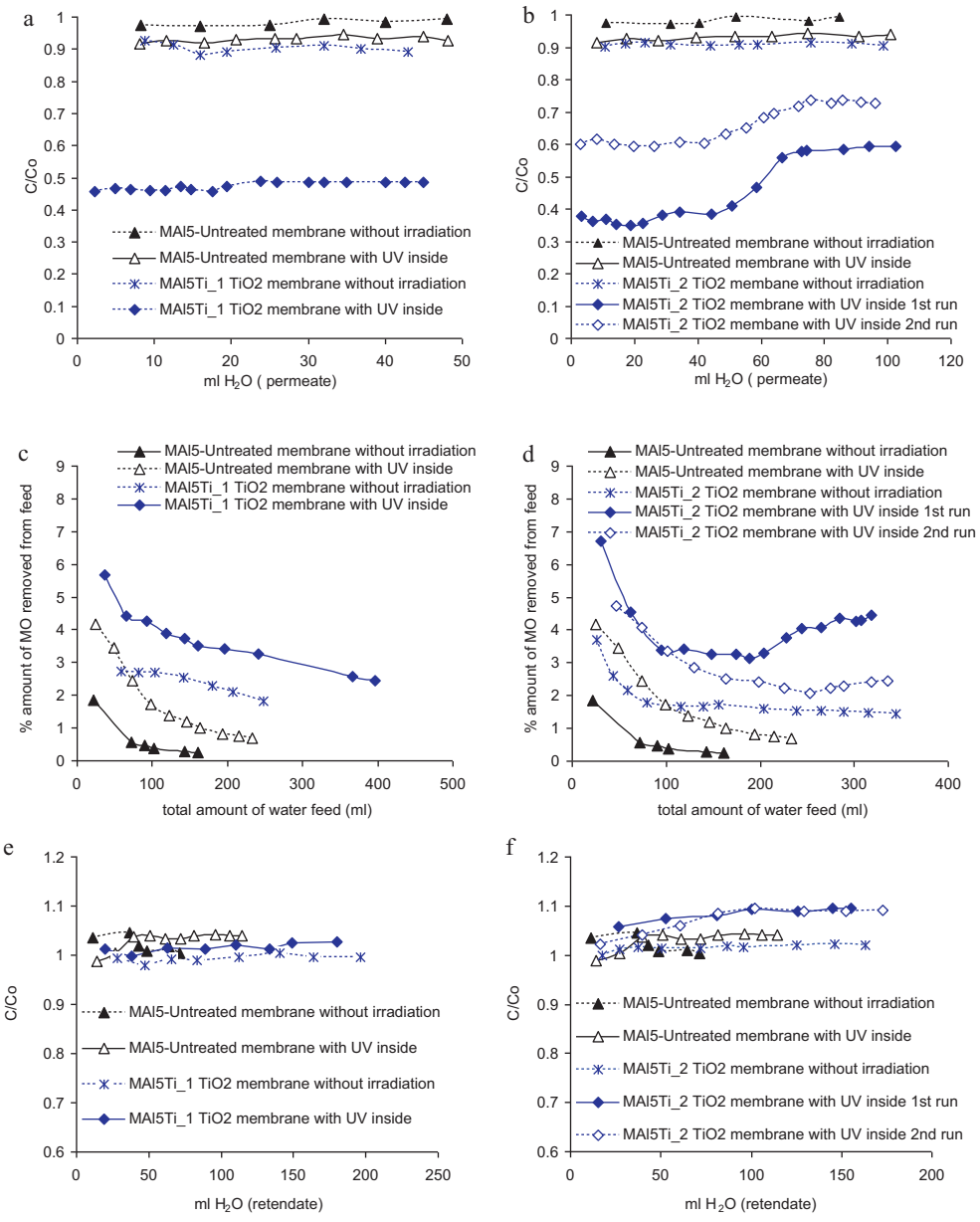

Fig. 9. Efficiency of the NPG developed TiO_2 membranes MAl5Ti_1 and MAl5Ti_2 to photo degrade MO in the continuous flow mode with internal irradiation in comparison with the untreated membrane MAl5: (a) Permeate concentration for membrane MAl5Ti_1, (b) Permeate concentration for membrane MAl5Ti_2, (c) MAl5Ti_1, % amount of MO removed from the feed, (d) MAl5Ti_2, % amount of MO removed from the feed, (e) Retendate concentration for membrane MAl5Ti_1, (f) Retendate concentration for membrane MAl5Ti_2.

Table 3
Discrimination between the amounts removed by photolysis, adsorption on alumina, adsorption on titania and photodegradation on titania.

	Differential pressure/total flow/permeate flow (atm)/(ml min^{-1})/(ml min^{-1})	Total removed MO up to a solution feed of: 150 ml/250 ml (μg)	Mass TiO_2: internal/external/total (mg)	Net mass of MO degraded up to a solution feed of: 150 ml/250 ml (μg)	Net mass of MO adsorbed up to a solution feed of: 150 ml/250 ml (μg)
MAl5 control	14.7/1.5/0.39	2.6/2.6	0		2.6/2.6
MAl5 UV inside	14.4/1.5/0.42	10.4/10.4	0	7.8/7.9	
MAl5Ti_1 control	13.6/1.5/0.13	22/28	12/37/49		19.4/25.4
MAl5Ti_1 UV inside	13.4/1.5/0.16	36.4/53	–/–	14.4/25	
MAl5Ti_2 control	14.2/1.5/0.21	17.5/24	23/25/48		14.9/21.4
MAl5Ti_2 UV inside	13.8/1.5/0.25	32/63	–/–	14.5/39	

of MO must have been removed since there is again an indication of MO concentration increase at almost identical permeate volume (Fig. 9b).

After subtracting the photolysis effect (MAl5 UV inside, Table 3), it was found that the internal surface of membrane MAl5Ti_2 photodegraded 39–7.9 = 31.1 μg of MO while the respective amount for membrane MAl5Ti_1 was 25–7.9 = 17.1 μg. These results proclaim the similar photodegradation efficiency for the TiO_2 layers developed in the internal membrane side. Indeed, the photodegraded MO amount per mass of deposited TiO_2 for membranes MAl5Ti_2, MAl5Ti_1 is 1.35×10^{-3} and 1.425×10^{-3} g g^{-1} respectively. The identical photocatalytic activity is in consistency with the remark already discussed in Section 3.2, that the morphology of the internally deposited layers is independent of the applied CVD technique (cross-flow or flow-trough).

3.4.2. Irradiation of both sides

Fig. 10a shows that the continuous flow procedure became more efficient in photodegrading MO when illumination was applied on both membrane sides.

After passing 200 ml of the feed solution through the purification device, membrane MAl5Ti_2 takes off 4.3% of the MO from the feed solution while the relevant amount removed by irradiating solely its internal surface was 3.3%. Further evidence that the higher efficiency was the result of the external irradiation is given in Fig. 10c. It can be seen that during the test, the pollutant concentration at the retendate side of the membrane (external) was retained to a lower level than this obtained when UV illuminated just the internal surface. Moreover from Fig. 10b, it can be seen that the permeate concentration at the steady state is similar to this obtained during the first run with illumination on the internal surface and that the steady state photodegradation is reached from the first 20 ml of permeate due to the absence of adsorption on the external surface.

3.4.3. Permeability evolution

High flux and inherent anti-biofouling properties of the membranes are of highly importance in membrane based water treatment technology. It should be noted that the counterbalance between increasing the photocatalytic effectiveness by increasing the deposited amount and consequently decreasing the permeance must be thoroughly considered for ending up with an efficient and economically feasible photocatalytic process involving membranes. This issue may consist the subject of very intensive process engineering and optimization studies. For this reason, the effort in this work focused on the development of ultra thin photocatalytically active TiO_2 layers, possessing high porosity and enhanced hydrophilic character. As shown in Table 1, although the developed NPG layers were ultra thin (<5 μm), the TiO_2 membranes MAl5Ti_1, MAl5Ti_2, MAl5Ti_3, exhibited helium and nitrogen permeance values that were in the range of 13–22% of those measured for the respective unmodified membrane MAl5.

The water permeance was calculated according to the following equation:

$$\mathrm{Pe} = \frac{F_w}{S\Delta P} \times \rho_w \times \frac{1}{60}\left(\frac{\mathrm{min}}{\mathrm{s}}\right) \times \frac{1}{18}\left(\frac{\mathrm{mol}}{\mathrm{g}}\right) \times 10^4 \left(\frac{\mathrm{cm}^2}{\mathrm{m}^2}\right) \times \frac{1}{101,325}\left(\frac{\mathrm{atm}}{\mathrm{Pa}}\right) \quad (7)$$

where F_w (ml min^{-1}) the water flow measured at the permeate side of the membrane (inner channel), S (cm^2) the active surface of the membrane, ΔP (atm) the pressure difference between the outer and the inner channel of the cell unit and ρ_w the density of water at the temperature of measurement.

What is interesting to note is that the water permeance values of the developed membranes were in the range of 36–54% of the starting membrane in dark and 39–60% under UV irradiation. This difference between the gas permeance and water permeance reduction after the treatment is indicative for the higher photoinduced hydrophilicity of the developed TiO_2 layers compared to the γ-alumina. The difference between the water permeance in dark and under illumination is indicative for the occurrence of photo-induced hydrophilicity effects as observed in several recent

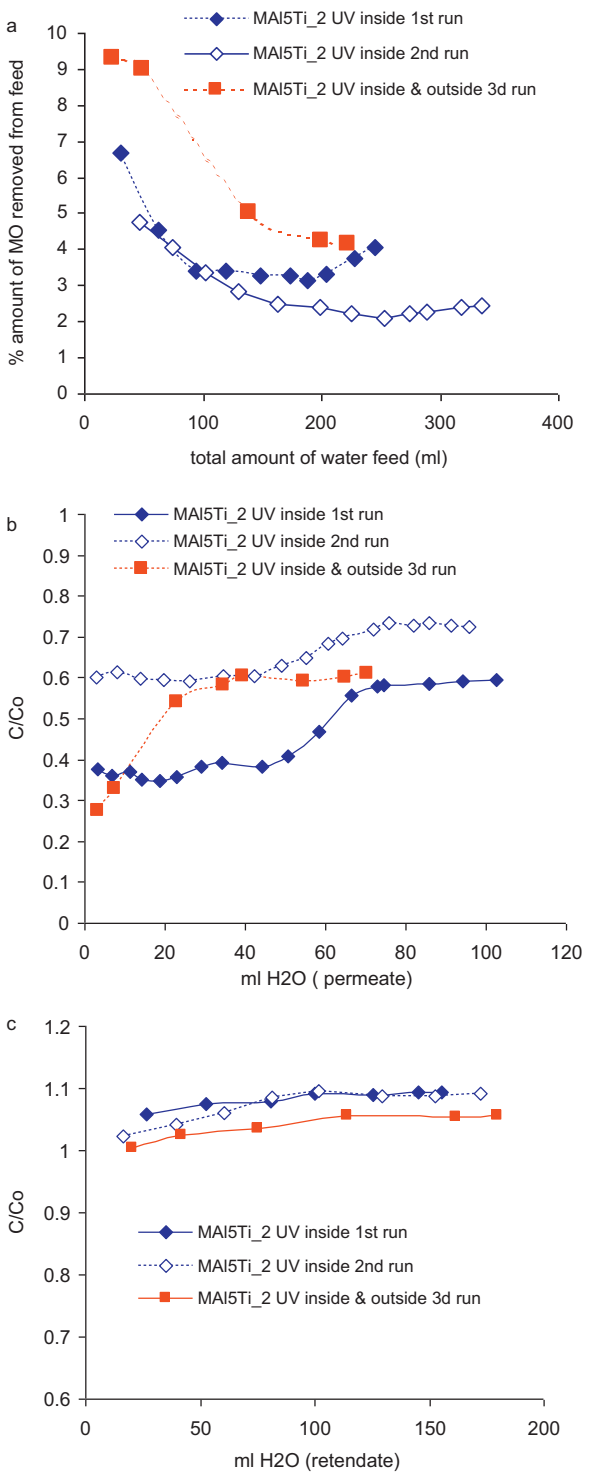

Fig. 10. Comparison between the experiments with irradiation on both surfaces and irradiation on the internal surface (a) % amount of MO removed from the feed, (b) concentration at the permeate side, (c) concentration at the retendate side.

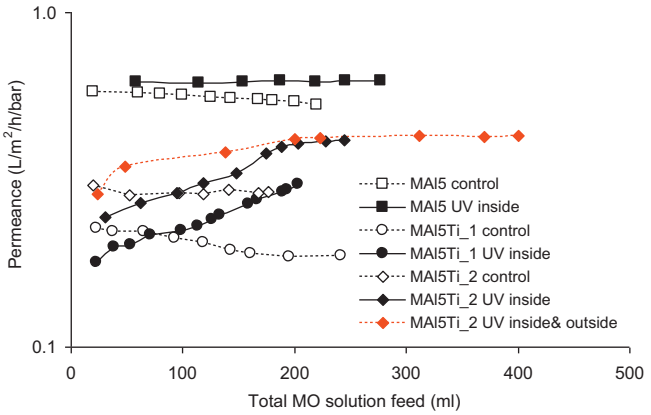

Fig. 11. The permeance evolution of the membranes during the control and illumination tests.

photocatalytic efficiency investigations [42]. The permeance evolution of the membranes during the photodegradation tests is explicitly presented in Fig. 11.

It can be observed that the NPG membranes irradiated by UV on their internal surface, exhibited flux increase rather than flux decline and no significant fouling formation over time, compared to the control experiments without UV. This difference is attributed to the photocatalytic and photolytic activity of the TiO_2/UV system. While organic contaminants attach at the internal TiO_2 membrane surface and interact to form an adsorption fouling layer in static condition, they are also attacked by the photocatalytic and photolytic action and thus the foulants are decomposed or their attachment strength is weakened.

More specific the unmodified γ-alumina membrane MAl5 exhibited a flux decline down to the 90% of the starting value during the control test whereas, photolysis under UV allowed for a stable permeance factor of 0.62 l m^{-2} h^{-1} bar^{-1}, up to a total feeding volume of 300 ml, which corresponds to about 3.5 h under of operation time. The respective flux decline for the modified membranes MAl5Ti_1 and MAl5Ti_2 in dark was down to 85% and 93% respectively while during the illuminated experiments their permeance was continuously increased both due to decomposition of the adsorbed pollutant and enhancement of the hydrophilicity induced by the UV irradiation. Interesting to note is that when membrane MAl5Ti_2 was irradiated on both its surfaces, it exhibited an abrupt increase of the water flux from the very beginning of the test and a permeance factor that was higher than this obtained in the absence of external irradiation. This is again an indication of MO adsorption occurring on the external TiO_2 layer during the tests performed in the absence of external irradiation.

4. Conclusions

The cross-flow CVD deposition of TiO_2 nanoparticles strongly depends on the conditions of the CVD reactor and especially on the temperature gradient between the gas phase and the membrane surface. In order to control uniformity of coating, it is necessary to ensure at least 1 °C higher gas phase temperature. In this way all of the developed in the gas phase TiO_2 nanoparticles are deposited on the membrane surface under the action of a positively acting thermophoretic driving force and extended consumption on cold surfaces downstream the CVD reactor is avoided. Under these conditions the coating thickness (amount/m^2) of the deposit is linearly proportional to the period of treatment whereas the particle size of the deposited nanoparticles depends on the temperature difference between the gas phase and the membrane surface that must not exceed the +5 °C to avoid the deposition of large particles with lower surface areas and thereby lower photocatalytic activity. The variance of temperature over the entire membrane length during pyrolysis does not affect the crystal structure as long as the temperature is above 400 °C. Moreover the particle size of the deposited TiO_2 depends strongly on the temperature difference rather than the absolute temperature of the reactor. Working temperatures of around 450 °C favoured the co-deposition of TiO_2 precursor that acts as a binding agent between the particles and between the particles and the underlying support ensuring better stability of the deposited layer. In this case the particles have a granular shape and at temperature differences of 3–5 °C in favour of the gas phase, optimum treatment periods may be well below 350 min.

The flow-through CVD techniques led to extended deposition of overgrown particles (200–500 nm) of either granular or crystalline shapes depending on the sign of the temperature gradient. At this point we should emphasise the advantage of in situ monitoring the permeability evolution during the CVD treatment, which allows for promptly control of the reactor conditions in order to enhance the deposition rate and improve the homogeneity of the deposited TiO_2 layer. Although improvement actions were not applied in this work, through this procedure it was possible to conclude the low extend of TiO_2 deposition during the cross-flow CVD on the external membrane surface, as the result of a counter to the deposition acting thermophoretic driving force.

Concerning the pollutant degradation efficiency of the membranes, this was for the first time investigated in a continuous flow rather a batch process. The results concluded to the point that double-side active TiO_2-modified membranes photodegraded almost double amount of a common pollutant like methyl orange, when operating in the common cross-flow membrane mode under UV irradiation of both sides. Under these conditions, the membranes exhibited high rate of purified water yield with no signs of fouling tendency. In addition, the novel photocatalytic membrane purification device provided the possibility to effectively illuminate with UV light each membrane surface (external and internal) separately and in this way it was possible to discriminate between the fractions of pollutant that were removed due to adsorption on the alumina substrate and the TiO_2 layer, due to photolysis and due to the TiO_2 photodegradation.

Acknowledgements

The research leading to these results has received funding from the European Union's Seventh Framework Programme (FP7/2007-2013) under Grant Agreement no 227017 ("Clean Water" collaborative project, co-funded by the Research DG of the European Commission within the joint RTD activities of the Environment and NMP Thematic Priorities).

Appendix A. Supplementary data

Supplementary data associated with this article can be found, in the online version, at doi:10.1016/j.jhazmat.2011.09.081.

References

[1] K. Sivonen, Cyanobacterial toxins, in: I. Chorus, J. Batram (Eds.), Toxic Cyanobacteria in Water: A guide to their Public Health Consequences, Monitoring and Management, WHO, E & FN Spon, London, 1999, p. 55.
[2] H. Choi, E. Stathatos, D.D. Dionysiou, Photocatalytic TiO_2 films and membranes for the development of efficient wastewater treatment and reuse systems, Desalination 202 (2007) 199–206.
[3] G. Owen, M. Bandi, J.A. Howell, S.J. Churchouse, Economic assessment of membrane processes for water and waste water treatment, J. Membr. Sci. 102 (1995) 77–91.
[4] H. Choi, H.-S. Kim, I.-T. Yeam, D.D. Dionysiou, Pilot plant study of an ultrafiltration membrane system for drinking water treatment operated in the feed-and-bleed mode, Desalination 172 (2005) 281–291.

[5] H. Choi, K. Zhang, D.D. Dionysiou, D.B. Oerther, G.A. Sorial, Effect of permeate flux and tangential flow on membrane fouling for wastewater treatment, Sep. Purif. Technol. 45 (2005) 68–78.
[6] Y.S. Lin, Microporous and dense inorganic membranes: current status and prospective, Sep. Purif. Technol. 25 (2001) 39–55.
[7] L.G.A. van de Water, T. Maschmeyer, Mesoporous membranes a brief overview of recent developments, Top. Catal. 29 (2004) 67–77.
[8] S.-Y. Kwak, S.H. Kim, S.S. Kim, Hybrid organic/inorganic reverse osmosis (RO) membrane for bactericidal anti-fouling. 1. Preparation and characterization of TiO_2 nanoparticle self-assembled aromatic polyamide thin-film-composite (TFC) membrane, Environ. Sci. Technol. 35 (2001) 2388–2394.
[9] D.-S. Bae, K.-S. Han, S.-H. Choi, Preparation and thermal stability of doped TiO_2 composite membranes by the sol–gel process, Solid State Ionics 109 (1998) 239–245.
[10] H. Choi, K. Zhang, D.D. Dionysiou, D.B. Oerther, G.A. Sorial, Influence of cross-flow velocity on membrane performance during filtration of biological suspension, J. Membr. Sci. 248 (2005) 189–199.
[11] S. Ciston, R.M. Lueptow, K.A. Gray, Controlling biofilm growth using reactive ceramic ultrafiltration membranes, J. Membr. Sci. 342 (2009) 263–268.
[12] T.V. Gestel, C. Vandecasteele, A. Buekenhoudt, C. Dortemont, J. Luyten, R. Leysen, B.V.D. Bruggen, G. Maes, Alumina and titania multilayer membranes for nanofiltration: preparation, characterization and chemical stability, J. Membr. Sci. 207 (2002) 73–89.
[13] C.-Y. Tsai, S.-Y. Tam, Y. Lu, J. Brinker, Dual-layer asymmetric microporous silica membranes, J. Membr. Sci. 169 (2000) 255–268.
[14] A.J. Burggraaf, L. Cot, General overview, trends and prospects, in: A.J. Burggraaf, L. Cot (Eds.), Fundamentals of Inorganic Membrane Science and Technology, Elsevier, Amsterdam, The Netherlands, 1996, pp. 1–20.
[15] A. Alem, H. Sarpoolaky, M. Keshmiri, Titania ultrafiltration membrane: Preparation, characterization and photocatalytic activity, J. Eur. Ceram. Soc. 29 (2009) 629–635.
[16] H. Choi, A.C. Sofranko, D.D. Dionysiou, Nanocrystalline TiO_2 photocatalytic membranes with a hierarchical mesoporous multilayer structure: Synthesis, characterization, and multifunction, Adv. Funct. Mater. 16 (2006) 1067–1074.
[17] A. Lambropoulos, G. Romanos, Th. Steriotis, J. Nolan, F. Katsaros, E. Kouvelos, G. Charalambopoulou, N. Kanellopoulos, Application of an innovative mercury intrusion technique and relative permeability to examine the thin layer pores of sol–gel and CVD post-treated membranes, Microporous Mesoporous Mater. 99 (2007) 206–215.
[18] S.F. Nitodas, E.P. Favvas, G.E. Romanos, M.A. Papadopoulou, A.Ch. Mitropoulos, N.K. Kanellopoulos, Development and characterization of silica-based membranes for hydrogen separation, J. Porous Mater. 15 (2008) 551–557.
[19] A.I. Labropoulos, G.E. Romanos, G.N. Karanikolos, F.K. Katsaros, N.K. Kakizis, N.K. Kanellopoulos, Comparative study of the rate and locality of silica deposition during the CVD treatment of porous membranes with TEOS and TMOS, Microporous Mesoporous Mater. 120 (2009) 177–185.
[20] A.I. Labropoulos, G.E. Romanos, N. Kakizis, G.I. Pilatos, E.P. Favvas, N.K. Kanellopoulos, Investigating the evolution of N_2 transport mechanism during the cyclic CVD post-treatment of silica membranes, Microporous Mesoporous Mater. 110 (2008) 11–24.
[21] Y. Gu, S.T. Oyama, Permeation properties and hydrothermal stability of silica–titania membranes supported on porous alumina substrates, J. Membr. Sci. 345 (2009) 267–275.
[22] U. Backman, A. Auvinen, J.K. Jokiniemi, Deposition of nanostructured titania films by particle-assisted MOCVD, Surf. Coat. Technol. 192 (2005) 81–87.
[23] F.-D. Duminica, F. Maury, F. Senocq, Atmospheric pressure MOCVD of TiO_2 thin films using various reactive gas mixtures, Surf. Coat Technol. 188–189 (2004) 255–259.
[24] Z. Ding, X. Hub, P.L. Yue, G.Q. Lu, P.F. Greenfield, Synthesis of anatase TiO_2 supported on porous solids by chemical vapor deposition, Catal. Today 68 (2001) 173–182.
[25] G. Li Puma, A. Bono, D. Krishnaiah, J.G. Collin, Preparation of titanium dioxide photocatalyst loaded onto activated carbon support using chemical vapor deposition: A review paper, J. Hazard. Mater. 157 (2008) 209–219.
[26] Y.H. Wang, X.Q. Liu, G.Y. Meng, Preparation and properties of supported 100% titania ceramic membranes, Mater. Res. Bull. 43 (2008) 1480–1491.
[27] R. Molinari, C. Grande, E. Drioli, L. Palmisano, M. Schiavello, Photocatalytic membrane reactors for degradation of organic pollutants in water, Catal. Today 67 (2001) 273–279.
[28] H. Shao, M.C. Chang, R.Y. Horng, Photocatalytic reaction Systems for Water Purification, US2009/0148359 A1.
[29] G.M. Carmignani, L.W. Frederick, Apparatus and Method for Photocatalytic Purification and Dissinfection of Water and Ultrapure Water, WO 02/083570 A1.
[30] O.C. Vangeli, G.E. Romanos, K.G. Beltsios, D. Fokas, C.P. Athanasekou, N.K. Kanellopoulos, Development and characterization of chemically stabilized ionic liquid membranes-Part I: Nanoporous ceramic supports, J. Membr. Sci. 365 (2010) 366–377.
[31] F. Maury, F.-D. Duminica, F. Senocq, Optimization of the vaporization of liquid and solid CVD precursors: Experimental and modeling approaches, Chem. Vap. Deposition 13 (2007) 638–643.
[32] S. Seifried, M. Winterer, H. Hahn, Nanocrystalline titania films and particles by chemical vapor synthesis, Chem. Vap. Deposition 6 (2000) 239–244.
[33] P. Falaras, G. Romanos, P. Aloupogiannis, Photocatalytic Purification Device, Application number EP10275076.7.
[34] S. Kelly, F.H. Pollak, M. Tomkiewicz, Raman spectroscopy as a morphological probe for TiO_2 aerogels, J. Phys. Chem. B 101 (1997) 2730–2734.
[35] V. Likodimos, T. Stergiopoulos, P. Falaras, J. Kunze, P. Schmuki, Phase composition, size, orientation, and antenna effects of self-assembled anodized titania nanotube arrays: A polarized micro-Raman investigation, J. Phys. Chem. C 112 (2008) 12687–12696.
[36] D.G. Huizenga, D.M. Smith, Knudsen diffusion in random assemblages of uniform spheres, AlChE J. 32 (1986), No 1.
[37] Y. Sun, A. Li, M. Qi, L. Zhang, X. Yao, Effects of oxygen on the properties of titania nanoparticles prepared by MOCVD, J. Mater. Sci. 37 (2002) 1343–1346.
[38] H. Zhao, X. Liu, S.D. Tse, Effects of pressure and precursor loading in the flame synthesis of titania nanoparticles, J. Aerosol Sci. 40 (2009) 919–937.
[39] L. Tatti, D. Niego, F. Rota, P. Bruzzi, A. Moroni, I.R. Bellobono, Mathematical modelling of pilot-plant photominerilization of chlorophenols in aqueous solution, by photocatalytic membranes immobilizing titanium dioxide, Chemosphere 34 (1991) 41–49.
[40] A.O Ibhadon, G.M. Greenway, Y. Yue, P. Falaras, D. Tsoukleris, The photocatalytic activity and kinetics of the degradation of an anionic azo-dye in a UV irradiated porous titania foam, Appl. Catal. B: Environ. 84 (2008) 351–355.
[41] N. Guettai, H.A. Amar, Photocatalytic oxidation of methyl orange in presence of titanium dioxide in aqueous suspension. Part II: kinetics study, Desalination 185 (2005) 439–448.
[42] A.G. Kontos, M. Pelaez, V. Likodimos, N. Vaenas, D.D. Dionysiou, P. Falaras, Visible light induced wetting of nanostructured N–F co-doped titania films, Photochem. Photobiol. Sci. 10 (2011) 350–354.